Highly Efficient SnIn4S8@ZnO Z-Scheme Heterojunction Photocatalyst for Methylene Blue Photodegradation

Qiang Luo , Changlin Sun , Juan Zhao * , Qizhou Cai , Shanshan Yao

Posted Date: 24 August 2023

doi: 10.20944/preprints202308.1718.v1

Keywords: SnIn4S8@ZnO; Z-scheme heterojunction; hydrothermal synthesis; MB photodegradation doi:10.20944/preprints202308.1718.v1

Article

Highly Efficient $SnIn_4S_8$@ZnO Z-Scheme Heterojunction Photocatalyst for Methylene Blue Photodegradation

Qiang Luo [1], Changlin Sun [1], Juan Zhao [2],*, Qizhou Cai [3] and Shanshan Yao [4]

[1] School of Mechanical Engineering, Wuhan Polytechnic University, Wuhan 430048, China; luoqiangncwh30@163.com (Q.L.); 1435839673@qq.com (C.S.)
[2] School of Mathematics & Computer Science, Wuhan Polytechnic University, Wuhan 430048, China
[3] State Key Lab of Material Processing and Dies & Mould Technology, Huazhong University of Science and Technology, Wuhan 430074, China; caiqizhou@hust.edu.cn
[4] Research School of Advanced Materials, School of Materials Science and Engineering, Jiangsu University, Zhenjiang 212013, China; yaosshan@hotmail.com
* Correspondence: Lotus6J@163.com

Abstract: Building heterojunction is promising strategy for the achievement of highly efficient photocatalysis. Herein, a novel $SnIn_4S_8$@ZnO Z-scheme heterostructure with tight contact interface was successfully constructed by a convenient two-step hydrothermal approach. The phase composition, morphology, as well as photophysical characteristics of $SnIn_4S_8$@ZnO were investigated through a series of characterization methods, respectively. Methylene blue (MB) was chosen as the target contaminant for photocatalytic degradation. In addition, the degradation process was fitted with pseudo-first order kinetics. The as-prepared $SnIn_4S_8$@ZnO heterojunctions displayed excellent photocatalytic activities toward MB degradation. The optimized sample (ZS800), in which the molar ratio of ZnO to $SnIn_4S_8$ was 800, displayed the highest photodegradation efficiency toward MB (91%) after 20 min. Furthermore, the apparent rate constant of MB photodegradation using ZS800 (0.121 min^{-1}) was 2.2 times over that using ZnO (0.054 min^{-1}). The improvement of photocatalytic activity could be ascribed to the efficient spatial separation of photoinduced charge carriers through a Z-scheme heterojunction with intimate contact interface. The results in this paper will bring a novel insight into constructing excellent ZnO-based photocatalytic systems for wastewater purification.

Keywords: $SnIn_4S_8$@ZnO; Z-scheme heterojunction; hydrothermal synthesis; MB photodegradation

---

1. Introduction

With the rapid development of human society, the problem of pollution is becoming more and more serious, and people have adopted many methods to deal with the problem of pollution [1–3]. Photocatalytic technology, as a new low-consumption, renewable and non-secondary pollution solution to pollution problems, has received extensive attention from researchers [4–8]. Through the continuous efforts of researchers, the photocatalytic materials have been greatly expanded, including oxides and sulfides such as ZnO、CdS、$NiCo_2O_4$ and $CuInS_2$ [9–12], perovskite such as $CsPbCl_3$ [13], graphite-like phase g-C_3N_4 [14] and mono-elemental red phosphorus [15], and so on. Among numerous photocatalytic materials, ZnO is a promising photocatalyst because it possesses many excellent characteristics such as high electron mobility, low cost, nontoxicity and easy preparation [16,17]. However, it is very easy for photoinduced electrons and holes of ZnO to recombine, which brings the low quantum yield, thus limiting its photocatalytic activity. For purpose of inhibiting the recombination between the photoinduced electrons and holes in ZnO, the following methods have been investigated by researchers: (i) Doping metal or non-metallic ions into ZnO can change its electron-hole concentration, thereby inhibiting the recombination between the photoinduced electrons and holes [18,19]. However, it would be usually difficult for doping elements to be doped into the lattice of ZnO and improper doping will actually inhibit its activity. (ii) Deposition of noble metals, such as Pt, Ag and Au, on the surface of ZnO is a typical surface modification strategy for the improvement of its optical quantum efficiency [20,21]. However, the high cost of these precious metals is not conducive to the promotion and practical application of this technology. (iii) The technique of coupling ZnO with other semiconductors which possess proper energy bands will produce heterogeneous structures. The photoinduced charge carriers will be separated through directional transfer in the presence of potential difference or internal electric field generated by the heterojunction, which will result in the significant improvement of the photocatalytic efficiency of the ZnO [22,23]. Therefore, the construction of heterojunction is a very promising technology for facilitating the progress of ZnO photocatalytic research [24–26].

$Snln_4S_8$, a typical polymetallic sulphide, has shown great latent capacity in the fields of the photocatalysis due to its unique structure. The $SnIn_4S_8$ material has a primary structure of nanoparticles and a secondary structure of micron-sized monodisperse sphere constructed from primary structure. This novel structure has two huge advantages for the application in the field of photocatalysis: (i) the primary structure provides a large specific surface area to adsorb more dye molecules; (ii) the secondary and porous structure can act as a light scattering center to improve the utilization of light. So far, $Snln_4S_8$ has been successfully prepared and applied to photocatalytic degradation of organic pollutants [27]. Most notably，benefitting from appropriate structure of $Snln_4S_8$ energy band, the photocatalytic activities of some materials can be enhanced by building a heterojunction with $Snln_4S_8$ [28–30]. However, the investigation on the application of the $Snln_4S_8$/ZnO heterojunction in the field about photocatalytic degradation of effluent containing organic contaminant has not been reported yet.

As a common organic dye, methylene blue (MB) is one of the main components of wastewater from the printing and dyeing industry. The wastewater containing MB will cause serious ecological pollution and destruction. Furthermore, MB can result in adverse effects on human health, such as irreversible damage of the eyes, increased heart rate, vomiting, shock, unhealthy pallor, jaundice, and tissue necrosis. Therefore, how to degrade MB in wastewater has been the direction explored by many researchers.

In this work, for purpose of enhancing the photo quantum efficiency of ZnO, $SnIn_4S_8$@ZnO Z-scheme heterojunction was synthesized by a convenient two-step hydrothermal approach. Furthermore, the photocatalytic activity of $SnIn_4S_8$@ZnO was assessed through the degradation of MB under the irradiation of ultraviolet (UV) light.

2. Materials and Methods

2.1. Synthesis of ZnO

ZnO in the form of nanosheets was prepared by a simple hydrothermal process. $ZnCl_2$ aqueous solution (50 mL, 1 mol/L) and KOH aqueous solution (20 mL, 7.5 mol/L) were prepared, respectively. The above two solutions were mixed, agitated for 20 min, then poured into a stainless steel autoclave with Teflon-lining whose volume was 100 mL. Afterwards, the sealed autoclave was heated in the electric oven at 180°C for 10 h, and then naturally cooled to ambient temperature. Finally, the product was separated through centrifugation, washed several times using deionized water and anhydrous alcohol, dried at 60°C for 10 h, and then ground for the formation of ZnO powders.

2.2. Synthesis of $SnIn_4S_8$@ZnO heterojunction

The typical procedure for $SnIn_4S_8$@ZnO heterojunction synthesis was as follows. Firstly, 70 mL of anhydrous ethanol solution with a certain quantity of $SnCl_4{\cdot}5H_2O$ was prepared. Secondly, a certain quantity of $InCl_3{\cdot}4H_2O$ was dissolved in the solution which was stirred for 10 min. Thirdly, 2.0345g of the as-prepared ZnO was mixed into the solution which was agitated for 20 min. Fourthly, a certain quantity of CH_4N_2S was mixed into the solution which was agitated for 20 min. Fifthly, the solution was poured into a stainless steel autoclave with Teflon-lining whose volume was 100 mL, the sealed autoclave was heated in an electric oven at 160°C for 10 h and then naturally cooled to ambient temperature. Finally, the products were washed using deionized water, dehydrated under vacuum at 70°C for 10 h, and then ground for further use. The obtained samples were recorded as

ZSX (X = 200, 400, 600, 800, and 1000), where X represented the molar ratio of ZnO to $SnIn_4S_8$. In addition, $SnIn_4S_8$ was prepared through the same approach mentioned above except addition of as-synthesized ZnO. The flow chart of the synthesis of the $SnIn_4S_8$, ZnO and $SnIn_4S_8$@ZnO samples is exhibited in Figure 1.

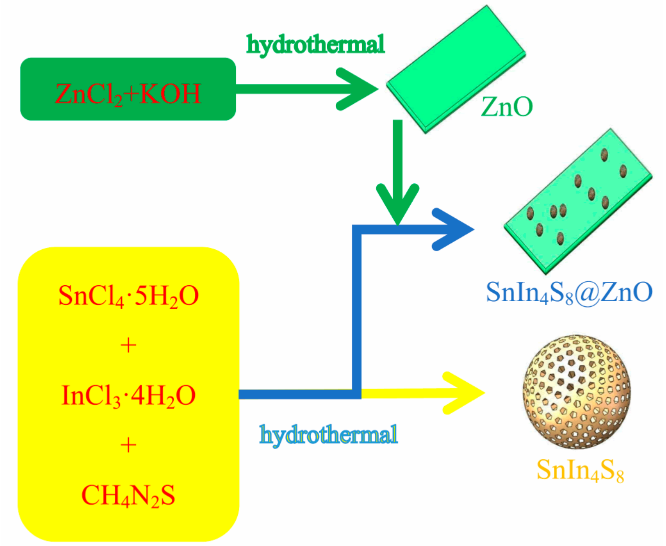

Figure 1. Synthesis chart of $SnIn_4S_8$, ZnO and $SnIn_4S_8$@ZnO.

2.3. Characterizations

The phase compositions of the as-synthesized samples were analyzed via an X-ray diffractometer (XRD, Rigaku Smartlab3kw, Japan). The morphologies of the samples were described using a field emission scanning electron microscope (FESEM, Zeiss Sigma 300, Germany) and a transmission electron microscope (TEM, FEI Titan G2 60-300, US). The distribution of elements was analyzed through energy dispersive X-ray (EDX) detector (Oxford X-Max, UK) which was merged into the FESEM. A UV-visible spectrophotometer (Shimadzu UV-2550, Japan) was used to characterize the absorption spectra of specimens. A fluorescence spectrophotometer (Lengguang Tech. F97XP, China) was used to test the photoluminescence (PL) spectra of specimens.

2.4. Photocatalytic degradation of MB

The photocatalytic efficiencies of specimens were evaluated through choosing MB as model pollutant. 15 mg of catalyst powders were added into MB solution (100 mL, 10 mg/L). The mixture was treated for 10 min through ultrasonic vibration and then agitated for 30 min in the dark to reach adsorption/desorption equilibrium. After that, the constantly stirred mixture was illuminated by an ultraviolet lamp whose power and irradiation peak wavelength was 36 W and 365 nm, respectively. 5 ml of the mixture was extracted at the interval of 5 min, and then the photocatalyst was removed through centrifugation. Finally, the UV-Vis spectrophotometer was used to determine the absorbance of solution at 664 nm.

3. Results and Discussion

3.1. XRD analysis

The XRD spectra of ZnO, $SnIn_4S_8$ and ZSX with a scanning speed of 10°/min are displayed in Figure 2a. Among them, the characteristic peaks of ZnO can correspond to (100), (002), (101), (102), (110), (103), (200), (112), (201), (004), and (202) crystalline facets of the hexagonal wurtzite phase of ZnO (JCPDS card No. 36-1451) [31]. The characteristic peaks of $SnIn_4S_8$ at $2\theta = 18.7°$, 28.6°, 33.2°, 48.3° and 50.1°, which are consistent with the (202), (222), (400), (440) and (531) crystal faces of cubic phase of $SnIn_4S_8$ (JCPDS card No. 42-1305), separately, can be observed [32]. Furthermore, no characteristic peaks of any foreign substance can be found in the XRD spectra, suggesting an excellent purity of the as-prepared $SnIn_4S_8$. In addition, the characteristic peaks of ZSX samples can be ascribed to the diffraction planes of ZnO (JCPDS card No. 36-1451). However, no diffraction peaks corresponding to $SnIn_4S_8$ can be found in the XRD patterns of ZSX samples, which should be attributed to the low level of $SnIn_4S_8$ in ZSX specimens and relatively fast scanning rate of XRD. In order to verify the existence of $SnIn_4S_8$ in ZSX samples, the as-prepared ZS1000 was test through XRD with a scanning rate of 4°/min and the pattern (Figure 2b) clearly displays that the diffraction peaks at 18.7° and 28.6° can be ascribed to (202) and (222) plane of $SnIn_4S_8$ (JCPDS card No. 42-1305).

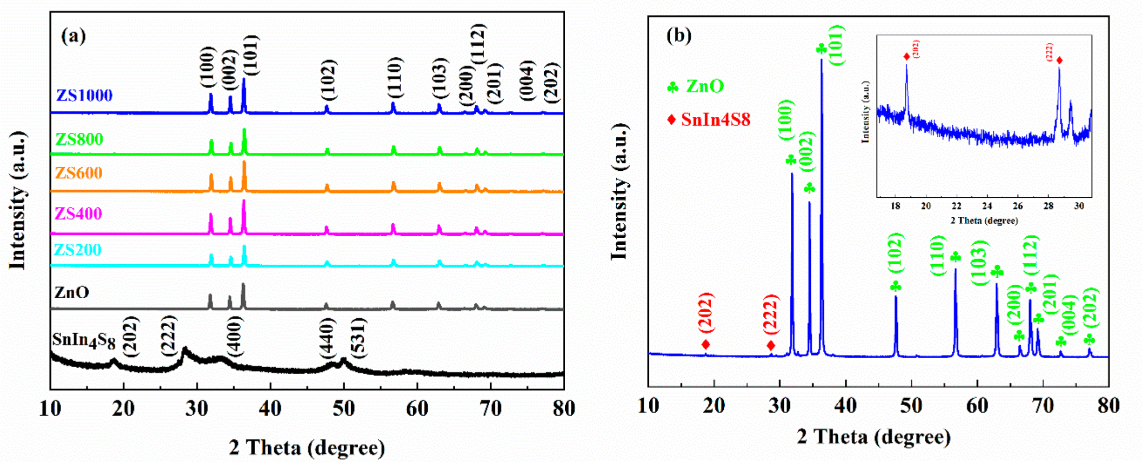

Figure 2. XRD spectra of (a) ZnO, $SnIn_4S_8$, and ZSX (scanning rate of 10°/min) and (b) ZS1000 (scanning rate of 4°/min).

3.2. Morphological analysis

The FSEM photographs of ZnO, $SnIn_4S_8$ and ZSX samples are presented in Figure 3. It can be seen that the ZnO showed flaky morphology with smooth surface (Figure 3a). The as-prepared $SnIn_4S_8$ showed a morphology of 3D hierarchical reticular microspheres with diameters of 2-4 μm (Figure 3b,c). From the magnified FSEM picture, it can be observed that the microspheres were composed of many two-dimensional nanoflakes with a thickness of about 20 nm. Furthermore, the microspheres possessed a porous appearance because of the interlacing of nanoflakes. The SEM images of ZSX samples show that many $SnIn_4S_8$ nanoparticles were unevenly distributed on the surface of the ZnO Substrate (Figure 3d-h). Furthermore, the number of nanoparticles gradually decreased with the increase of the molar ratio of ZnO to $SnIn_4S_8$. Moreover, EDX elemental mapping analysis of ZS200 demonstrated that the elements Zn, O, Sn, In and S existed in ZSX samples (Figure 4), which can further suggest that the large flake-like substrates were ZnO and the small nanoparticles were $SnIn_4S_8$.

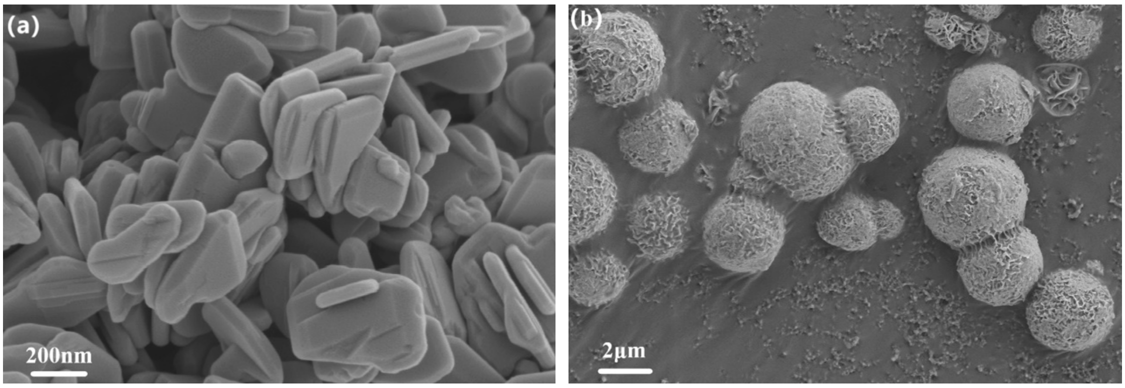

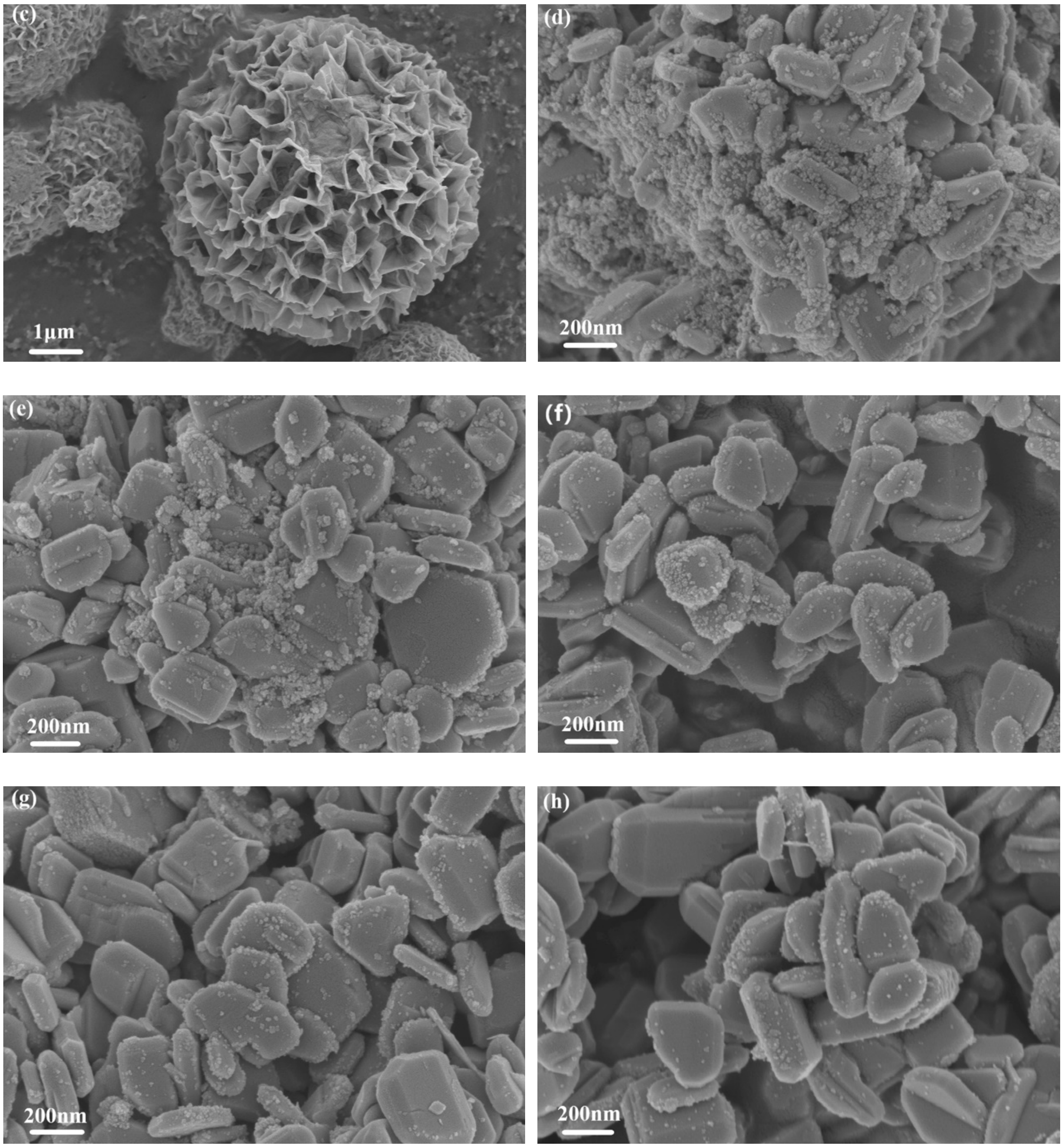

Figure 3. Microstructures of (a) pure ZnO nanosheets, (b,c) $SnIn_4S_8$ microspheres, (d) ZS200, (e) ZS400, (f) ZS600, (g) ZS800 and (h) ZS1000 heterostructures.

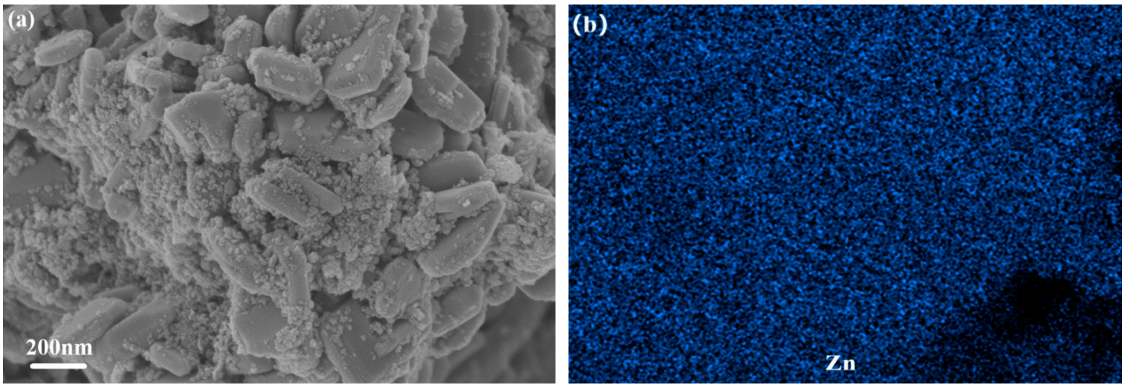

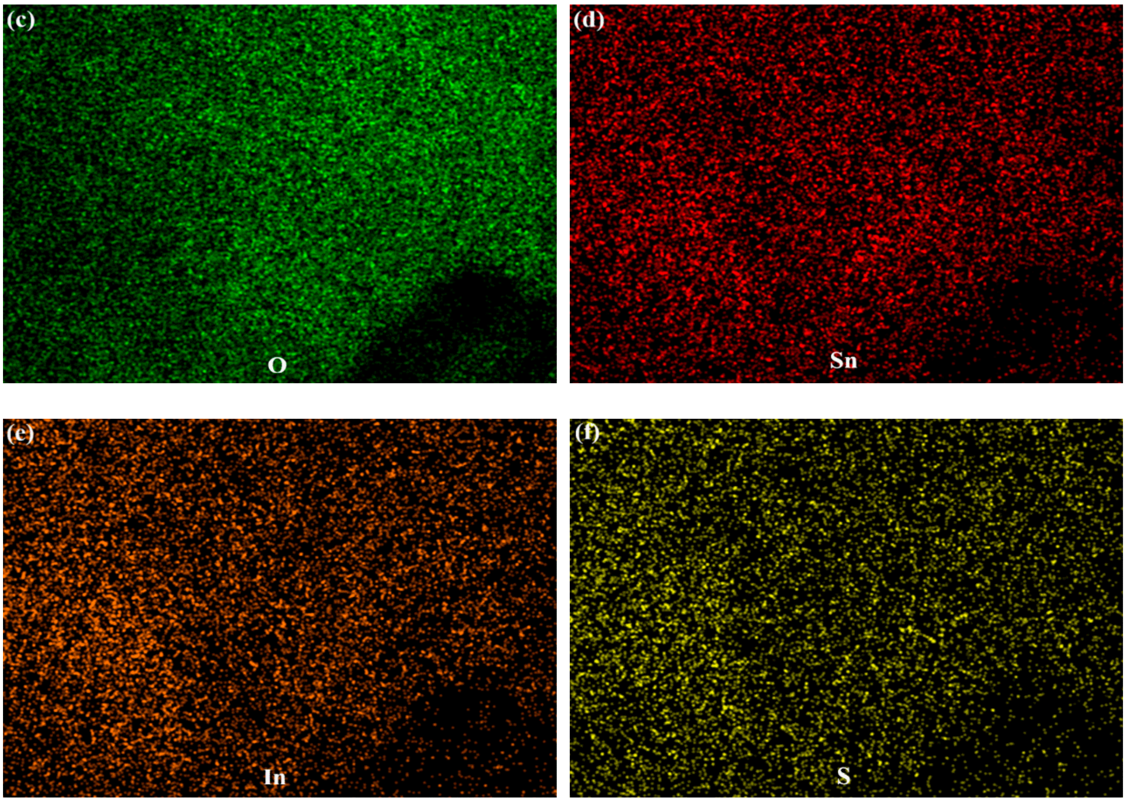

Figure 4. (a) Microstructure of ZS200 and (b-f) EDX elemental mapping images in the zone of (a).

The TEM photo of ZS800 obviously indicates that the $SnIn_4S_8$ nanoparticles densely covered the surface of the nanoflake-like ZnO to obtain the $SnIn_4S_8$@ZnO heterojunction (Figure 5a). Two kinds of lattice fringes are clearly displayed in HRTEM image of ZS800 , as shown in Figure 5b, the observed interplanar spacing of 0.247nm corresponded to ZnO (101) plane (JCPDS card No. 36-1451), and the characteristic interplanar spacing of 0.268nm belonged to $SnIn_4S_8$ (400) plane (JCPDS card No. 42-1305) [31,33]. Furthermore, it can be observed that the contact interface between ZnO and $SnIn_4S_8$ is very tight. The results mentioned above demonstrate that the $SnIn_4S_8$@ZnO heterojunction has been successfully constructed. The tight contact interface between $SnIn_4S_8$ and ZnO should be beneficial for the migration of photogenerated charge carriers and the stability of structure. As a consequence, the $SnIn_4S_8$@ZnO heterojunction would exhibit the enhanced photocatalytic activity.

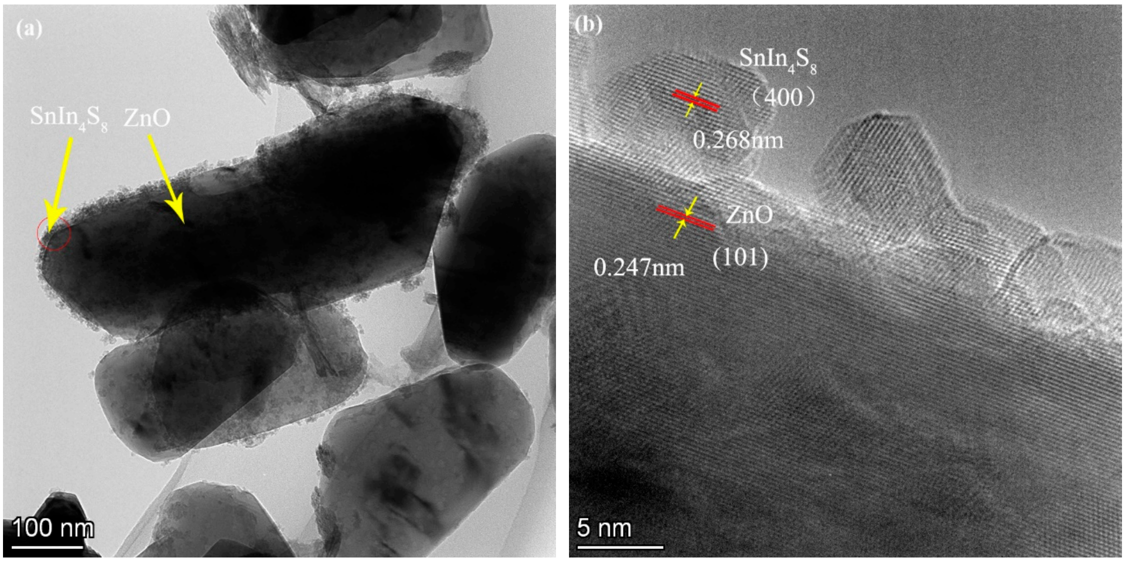

Figure 5. (a) TEM and (b) HRTEM photos of ZS800.

3.3. UV-Vis absorption spectra analysis

The light-harvesting ability can be regarded as a crucial factor for the photocatalytic activity of semiconductors. It can be found from the UV-vis absorption spectra (Figure 6a) that all the samples exhibited strong optical absorption in the region of UV. Moreover, the ZSX samples exhibited absorption cutoff wavelengths with slight redshift and the improvements of absorption capability in the Vis range compared to pure ZnO. The band gap (E_g) of the crystalline semiconductors can be obtained using the Kubelka:

$$\alpha hv = A(hv - E_g)^{n/2} \quad (1)$$

Where α is the absorbance, hv is the photon energy, and A is a constant [34]. The selection of n value (1 for direct transition, while 4 for indirect transition) is based on the transition property in the semiconductor [35]. The band gap energy of as-synthesized specimens was determined through selecting n as 1 because both $SnIn_4S_8$ and ZnO are direct transition semiconductors. Figure 6b presents the $(\alpha hv)^2$ curves with hv of ZnO and ZS800, the band gaps can be calculated through lengthening the linear portion to the x-axis, which indicates that the band gaps of ZnO and ZS800 were about 3.22eV and 3.19eV, respectively. The narrowing of bandgap energy suggested that light-harvesting capability of ZnO was improved by the hybridization with $SnIn_4S_8$.

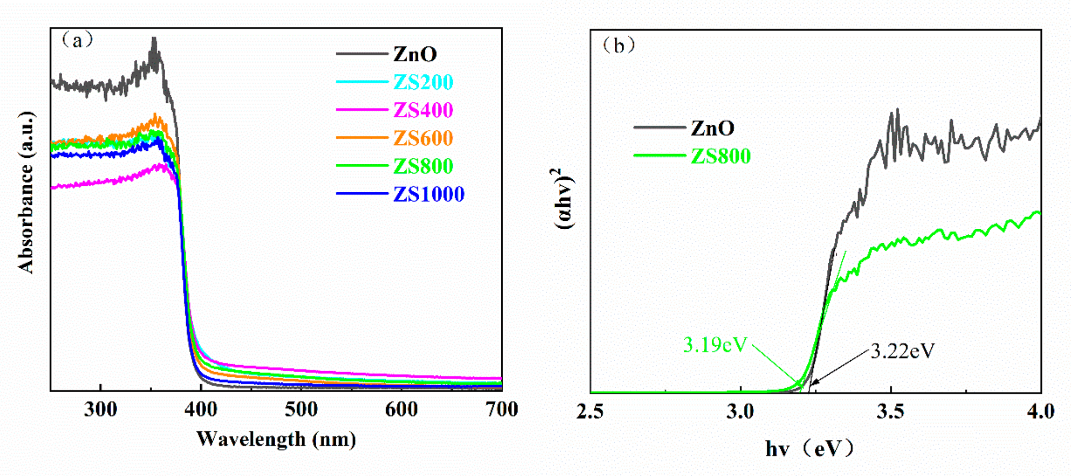

Figure 6. (a) UV-vis absorption spectra of ZnO and ZSX. (b) curves of $(\alpha hv)^2$ versus hv of ZnO and ZS800.

3.4. PL spectra analysis

The recombination rate of photoinduced charge carriers can be reflected through the peak intensity of PL spectrum. Normally, a weaker peak intensity reflects a higher separation efficiency of the photogenerated charge carriers, which results in a better photocatalytic performance [36,37]. The PL spectra of the as-synthesized ZnO and ZSX specimens are displayed in Figure 7, which reveals that all specimens had similar PL spectra with two distinct luminescence peaks at approximate 400 and 460 nm. The peak at about 400 nm was the emission near the edge of the band, which originated from the recombination of the free-excitons through the collision between the excitons, and the peak at about 460nm may be the result from the inherent defects of ZnO [38,39]. Furthermore, compared with ZnO, the intensity of the fluorescence spectra of ZSX samples were significantly reduced. It indicated that $SnIn_4S_8$@ZnO heterojunction had a lower recombination rate of photogenerated charge carriers, which would be beneficial for the improvement of photocatalytic performance of catalyst [40].

doi:10.20944/preprints202308.1718.v1

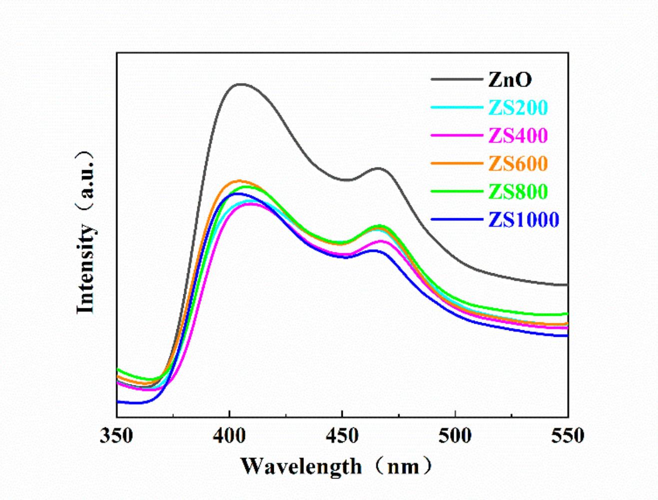

Figure 7. PL spectra of ZnO and ZSX.

3.5. Photocatalytic activities of the specimens

The MB photodegradation curves over ZnO and ZSX samples are shown in Figure 8a, and the ultimate degradation rates of MB after 20 min are exhibited in Figure 8b. The changes of MB concentrations were very small when MB was adsorbed for 30 min using all samples in the dark, which indicated that the adsorption effects of the ZnO and ZSX samples on MB were negligible. After 20 min of UV illumination, the degradation rates of MB degraded by ZnO, ZS200, ZS400, ZS600, ZS800 and ZS1000 were 66%, 88%, 88%, 86%, 91% and 87%, respectively. Compared with the ZnO, the ZSX samples exhibited obviously improved photocatalytic activities. Furthermore, ZS800 had the highest photocatalytic efficiency for MB degradation.

Generally speaking, the photodegradation of MB complies with the pseudo-first-order kinetic equation:

$$\ln\left(\frac{C_0}{C_t}\right) = kt \tag{2}$$

Where k, t, C_0, and C_t are the apparent rate constant, the photocatalytic reaction time, the MB concentrations at the moment of t = 0 and a certain time, respectively [41]. The kinetic curves of MB photodegradation in presence of ZnO and ZSX samples were fitted by plotting $\ln(C_0/C_t)$ versus time (Figure 8c), and the good inear relationship can be observed. The gradient of kinetic curve denotes k value which corresponds to the degradation efficiency. The k values of MB degradation over ZnO, ZS200, ZS400, ZS600, ZS800 and ZS1000 were 0.054, 0.108, 0.109, 0.101, 0.121 and 0.102 min^{-1}, separately (Figure 8d). It can be found that k value of ZSX samples for MB degradation were obviously higher than that of ZnO. Furthermore, ZS800 had the highest k value which was approximately 2.2 times over that of ZnO. These results indicate that the photocatalytic activity of the ZnO can be significantly boosted through hybridization with $SnIn_4S_8$ for the formation of $SnIn_4S_8$@ZnO heterojunction which is an efficient photocatalyst.

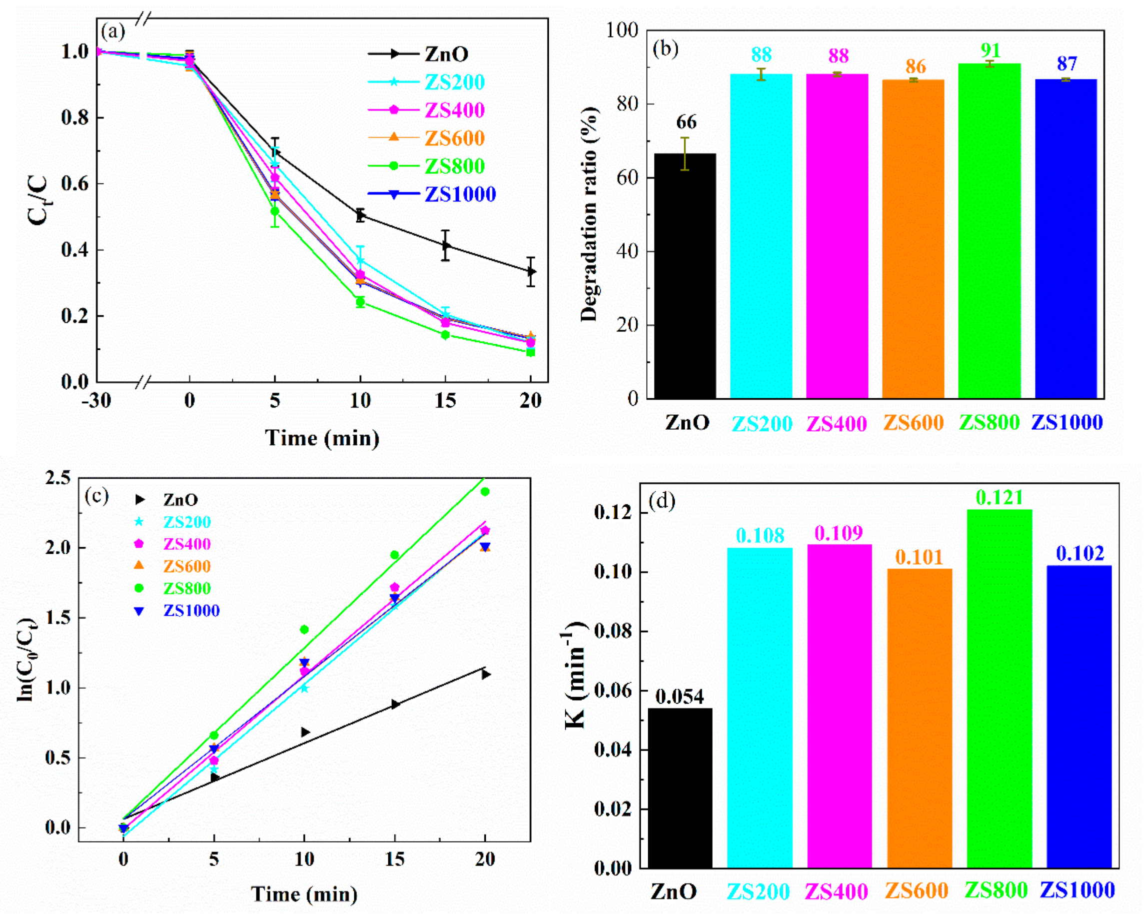

Figure 8. (a) Degradation curves of MB solution, (b) ultimate degradation rates of MB after 20 min, (c) kinetic curves of MB degradation and (d) calculated k values of MB degradation.

3.6. Photocatalytic mechanism analysis

According to the results in this work and several previous investigations, a Z-scheme mechanism can be proposed for efficient degradation of MB by the $SnIn_4S_8$@ZnO heterojunction, as shown in Figure 9. The previous investigations indicate that the conduction band (CB) position of $SnIn_4S_8$ is higher than that of ZnO, while the valence band (VB) position of ZnO is lower than that of $SnIn_4S_8$ [42–44]. Under the irradiation of UV light, the photoinduced electrons can transfer from the VB of the ZnO and $SnIn_4S_8$ to the CB of them, respectively, keeping the photogenerated holes in the VB of them. Then the photoinduced electrons in the CB of the ZnO can migrate to the VB of the $SnIn_4S_8$ owing to the appropriate potential difference. Eventually, a Z-shaped migration path of photogenerated electrons is formed in the $SnIn_4S_8$@ZnO heterojunction. This mechanism results that the photoinduced electrons collect in CB of $SnIn_4S_8$ while the photoinduced holes gather in VB of ZnO. These photoexcited electrons and holes are efficiently separated in the opposite side of $SnIn_4S_8$@ZnO heterojunction. Therefore, the life span of photo-induced carriers can be greatly improved, leading to remarkable improvement of photocatalytic activity. The photoinduced holes in VB of ZnO are vital oxidants, they can quickly oxidize hydroxyl anions (OH^-) to hydroxyl radicals (·OH). The photogenerated electrons in CB of $SnIn_4S_8$ are robust reductants, they can rapidly reduce dissolved oxygen (O_2) into superoxide radicals ($\cdot O_2^-$). Finally, the MB molecules can be degraded into the inorganic small molecules by these highly active ·OH and $\cdot O_2^-$ species. Overall, the main reactions of this mechanism can be expressed as below.

(1) $\mathrm{ZnO/SnIn_4S_8} + \mathrm{hv} \rightarrow \mathrm{ZnO(h^+(VB) + e^-(CB))/SnIn_4S_8\ (h^+(VB) + e^-(CB))}$
(2) $\mathrm{ZnO(h^+(VB) + e^-(CB))/SnIn_4S_8\ (h^+(VB) + e^-(CB))} \rightarrow \mathrm{ZnO(h^+(VB))} + \mathrm{SnIn_4S_8\ (e^-(CB))}$
(3) $\mathrm{ZnO(h^+(VB))} + \mathrm{OH^-} \rightarrow \cdot \mathrm{OH}$
(4) $\mathrm{SnIn_4S_8\ (e^-(CB))} + \mathrm{O_2} \rightarrow \cdot \mathrm{O_2^-}$
(5) $\cdot \mathrm{OH}, \cdot \mathrm{O_2^-} + \mathrm{MB} \rightarrow$ inorganic small molecules

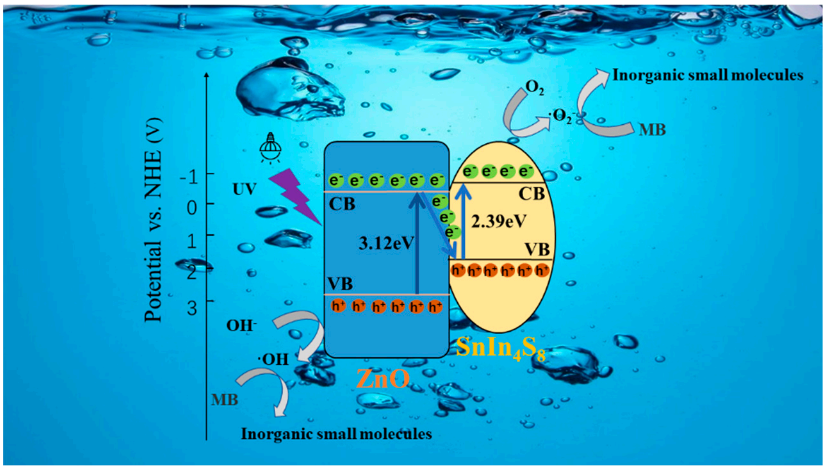

Figure 9. Sketch map of the carriers migration and photocatalysis.

4. Conclusions

In this work, $SnIn_4S_8$@ZnO Z-scheme heterojunction photocatalyst was successfully acquired through a convenient two-step hydrothermal approach. The as-synthesized $SnIn_4S_8$@ZnO exhibited significantly enhanced photocatalysis activity under UV light irradiation. The degradation ability of the $SnIn_4S_8$@ZnO structure towards MB was significantly stronger than that of pure ZnO. The remarkable performance for MB photodegradation can be ascribed to the efficient spatial separation of photoinduced electrons and holes through a Z-scheme heterojunction with intimate contact interface. To conclude, the results in this paper will bring a novel insight into constructing excellent ZnO-based photocatalytic systems for wastewater purification.

Author Contributions: Conceptualization, Q.L. and C.S.; methodology, Q.C. and S.Y.; software, C.S. and J.Z.; data curation, C.S.; writing—original draft preparation, Q.L. and C.S.; writing—review and editing, Q.L. and J.Z.; supervision, J.Z. All authors have read and agreed to the published version of the manuscript.

Funding: This research was funded by the Open Foundation of State Key Laboratory of Materials Processing and Die & Mould Technology, Huazhong University of Science and Technology, grant number P2023-028.

Institutional Review Board Statement: Not applicable.

Informed Consent Statement: Not applicable.

Data Availability Statement: The data presented in this study are available on request from the corresponding author.

Conflicts of Interest: The authors declare no conflict of interest.

References

1. Mali, H.; Shah, C.; Raghunandan, B.H.; Prajapati, A.S.; Patel, D.H.; Trivedi, U.; Subramanian, R.B. Organophosphate pesticides an emerging environmental contaminant: Pollution, toxicity, bioremediation progress, and remaining challenges. *J. Environ. Sci.* **2023**, 127, 234-250.
2. Zhang, S.; Yang, B.; Sun, C. Can payment vehicle influence public willingness to pay for environmental pollution control? Evidence from the CVM survey and PSM method of China. *J. Clean. Prod.* **2022**, 365, 132648.
3. Zhang, R.; Zhang, A.; Yang, Y.; Cao, Y.; Dong, F.; Zhou, Y. Surface modification to control the secondary pollution of photocatalytic nitric oxide removal over monolithic protonated g-C_3N_4/graphene cxide aerogel. *J. Hazard. Mater.* **2020**, 397, 122822.
4. Nuño, M.; Pesce, G.L.; Bowen, C.R.; Xenophontos, P.; Ball, R.J. Environmental performance of nano-structured $Ca(OH)_2/TiO_2$ photocatalytic coatings for buildings. *Build. Environ.* **2015**, 92, 734-742.
5. Tsang, C.H.A.; Li, K.; Zeng, Y.; Zhao, W.; Zhang, T.; Zhan, Y.; Xie, R.; Leung, D.Y.C.; Huang, H. Titanium oxide based photocatalytic materials development and their role of in the air pollutants degradation: overview and forecast. *Environ. Int.* **2019**, 125, 200-228.

6. Naghizadeh, M.; Taher, M.A.; Tamaddon, A.M. Facile synthesis and characterization of magnetic nanocomposite ZnO/$CoFe_2O_4$ hetero-structure for rapid photocatalytic degradation of imidacloprid. *Heliyon* **2019**, 5, e02870.
7. Xu, J.; Wen, Q.; Zhang, X.; Li, Y.; Cui, Z; Li, P.; Pan, C. One-step construction of multi-walled CNTs loaded with Alpha-Fe_2O_3 nanoparticles for efficient photocatalytic properties. *Materials* **2021**, 14, 2820.
8. Huang, R.; Wu, J.; Zhang, M.; Liu, B.; Zheng, Z.; Luo, D. Strategies to enhance photocatalytic activity of graphite carbon nitride-based photocatalysts. *Mater. Design* **2021**, 210, 110040.
9. Das, A.; Nair, R.G. Effect of aspect ratio on photocatalytic performance of hexagonal ZnO nanorods. *J. Alloy. Compd.* **2020**, 817, 153277.
10. Bhavsar, K.S.; Labhane, P.K.; Dhake, R.B.; Sonawane, G.H. Solvothermal synthesis of activated carbon loaded CdS nanoflowers: Boosted photodegradation of dye by adsorption and photocatalysis synergy. *Chem. Phys. Lett.* **2020**, 744: 137202.
11. He, S.; Chai, J.; Lu, S.; Mu, X.; Liu, R; Wang, Q.; Chen, F.; Li, Y.; Wang, J.; Wang, B. Solution-phase vertical growth of aligned $NiCo_2O_4$ nanosheet arrays on Au nanosheets with weakened oxygen-hydrogen bonds for photocatalytic oxygen evolution. *Nanoscale* **2020**, 12, 6195-6203.
12. Chumha, N.; Pudkon, W.; Chachvalvutikul, A.; Luangwanta, T.; Randorn, C.; Inceesungvorn, B.; Ngamjarurojana, A.; Kaowphong, S. Photocatalytic activity of $CuInS_2$ nanoparticles synthesized via a simple and rapid microwave heating process. *Mater. Res. Express* **2020**, 7, 015074.
13. Gao, G.; Xi, Q.; Zhou, H.; Zhao,Y.; Wu, C.; Wang, L.; Guo, P.; Xu, J. Novel inorganic perovskite quantum dots for photocatalysis. *Nanoscale* **2017**, 9, 12032-12038.
14. Sewnet, A.; Alemayehu, E.; Abebe, M.; Mani, D.; Thomas, S.; Lennartz, B. Hydrothermal synthesis of heterostructured g-C_3N_4/Ag-TiO_2 nanocomposites for enhanced photocatalytic degradation of organic pollutants. *Materials* **2023**, 16, 5497.
15. Ding, K.; Wen, L.; Huang, S.; Li, Y.; Zhang, Y.; Lu, Y. Electronic properties of red and black phosphorous and their potential application as photocatalysts. *RSC Adv.* **2016**, 6, 80872-80884.
16. Kumar, S.; Dhiman, A.; Sudhagar, P.; Krishnan, V. ZnO-graphene quantum dots heterojunctions for natural sunlight-driven photocatalytic environmental remediation. *Appl. Surf. Sci.* **2018**, 447, 802-815.
17. Ren, T.; Jin, Z.; Yang, J.; Hu, R.; Zhao, F.; Gao, X.; Zhao, C. Highly efficient and stable p-$LaFeO_3$/n-ZnO heterojunction photocatalyst for phenol degradation under visible light irradiation. *J. Hazard. Mater.* **2019**, 377, 195-205.
18. Vaiano, V.; Iervolino, G.; Rizzo, L. Cu-doped ZnO as efficient photocatalyst for the oxidation of arsenite to arsenate under visible light. *Appl. Catal. B: Environ.* **2018**, 238, 471-479.
19. Li, D.; Huang, J.; Cao, L.; Li, J.; Ou Yang, H.; Yao, C. Microwave hydrothermal synthesis of Sr^{2+} doped ZnO crystallites with enhanced photocatalytic properties. *Ceram. Int.* 2014, 40, 2647-2653.
20. Zheng, X.; Zhang, Z.; Meng, S.; Wang, Y.; Li, D. Regulating charge transfer over 3D Au/ZnO hybrid inverse opal toward efficiently photocatalytic degradation of bisphenol A and photoelectrochemical water splitting. *Chem. Eng. J.* **2020**, 393, 124676.
21. Kuriakose, S.; Sahu, K.; Khan, S.A.; Tripathi, A.; Avasthi D.K.; Mohapatra, S. Facile synthesis of Au-ZnO plasmonic nanohybrids for highly efficient photocatalytic degradation of methylene blue. *Opt. Mater.* **2017**, 64, 47-52.
22. Ma, M.; Huang, Y.; Liu, J.; Liu, K.; Wang, Z.; Zhao, C.; Qu, S.; Wang, Z. Engineering the photoelectrochemical behaviors of ZnO for efficient solar water splitting. *J. Semicond.* **2020**, 41, 091702.
23. Anwer, H.; Mahmood, A.; Lee, J.; Kim, K.H.; Park, J.W.; Yip, A.C.K. Photocatalysts for degradation of dyes industrial effluents: Opportunities and challenges. *Nano Res.* **2019**, 12, 955-972.
24. Ma, D.; Shi, J.; Sun, D.; Zou, Y.; Cheng, L.; He, C.; Wang, H.; Niu, C.; Wang, L. Au decorated hollow ZnO@ZnS heterostructure for enhanced photocatalytic hydrogen evolution: The insight into the roles of hollow channel and Au nanoparticles. *Appl. Catal. B: Environ.* **2019**, 244, 748-757.
25. Ma, Q.; Han, X.; Lv K.; Dong, R.; Hang, Z.; Xin, B.; Zheng, K. Ultrasound-enhanced preparation and photocatalytic properties of graphene-ZnO nanorod composite. *Sep. Purif. Technol.* **2021**, 259, 118131.
26. Fu, Y.; Ren, Z.; Wu, J.; Li, Y.; Liu, W.; Li, P.; Xing, L.; Ma, J.; Wang, H.; Xue, X. Direct Z-scheme heterojunction of ZnO/MoS_2 nanoarrays realized by flowing-induced piezoelectric field for enhanced sunlight photocatalytic performances. *Appl. Catal. B: Environ.* **2021**, 285, 119785.
27. Yan, T.; Li, L.; Li, G.; Wang, Y.; Hu, W.; Guan, X. Porous $SnIn_4S_8$ microspheres in a new polymorph that promotes dyes degradation under visible light irradiation. *J. Hazard. Mater.* **2011**, 186, 272-279.
28. Wang, J.; Wang, B.; Zhang, W.; Xiao, Y.; Xu, H.; Liu, Y.; Liu, Z.; Zhang, J.; Jiang, Y. Visible-light-driven double-shell $SnIn_4S_8$/TiO_2 heterostructure with enhanced photocatalytic activity for MO removal and Cr(VI) cleanup. *Appl. Surf. Sci.* **2022**, 587, 152867.
29. Sun, M.; Li, F.; Su, M.; Wei, D.; Yang, Q.; Yan, T.; Li, D. Fabrication of MOF-derived tubular In_2O_3@$SnIn_4S_8$ hybrid: Heterojunction formation and promoted photocatalytic reduction of Cr(VI) under visible light. *J. Colloid Interf. Sci* **2021**, 596, 278-287.

30. Shi, H.; Zhao, Y.; Fan, J.; Tang, Z. Construction of novel Z-scheme flower-like $Bi_2S_3/SnIn_4S_8$ heterojunctions with enhanced visible light photodegradation and bactericidal activity. *Appl. Surf. Sci.* **2019**, 465, 212-222.
31. Raji, R.; Gopchandran, K.G. Plasmonic photocatalytic activity of ZnO: Au nanostructures: Tailoring the plasmon absorption and interfacial charge transfer mechanism. *J. Hazard. Mater.* **2019**, 368, 345-357.
32. Chen, C.; Shaya, J.; Polychronopoulou, K.; Golovko, V.B.; Tesana, S.; Wang, S.; Lu, C. Photocatalytic degradation of ethiofencarb by a visible light-driven $SnIn_4S_8$ photocatalyst. *Nanomaterials* **2021**, 11, 1325.
33. Li, H.; Song, W.; Cui, X.; Li, Y.; Hou, B.; Cheng, L.; Zhang, P. Preparation of $SnIn_4S_8/TiO_2$ nanotube photoanode and its photocathodic protection for Q235 carbon steel under visible light. *Nanoscale Res. Lett.* **2021**, 16, 10.
34. Song, N.; Zhang, S.; Zhong, S.; Su, X.; Ma, C. A direct Z-scheme polypyrrole/Bi_2WO_6 nanoparticles with boosted photogenerated charge separation for photocatalytic reduction of Cr (VI): Characteristics, performance, and mechanisms. *J. Clean. Prod.* **2022**, 337, 130577.
35. Xiao, T.; Tang, Z.; Yang, Y.; Tang, L.; Zhou, Y.; Zou, Z. In situ construction of hierarchical WO_3/g-C_3N_4 composite hollow microspheres as a Z-scheme photocatalyst for the degradation of antibiotics. *Appl. Catal. B: Environ.* **2018**, 220, 417-428.
36. Luo, Q.; Cai, Q.; Li, X.; Chen, X. Characterization and photocatalytic activity of large-area single crystalline anatase TiO_2 nanotube films hydrothermal synthesized on plasma electrolytic oxidation seed layers. *J. Alloy. Compd*. **2014**, 597, 101-109.
37. Zhu, G.; Li. X.; Wang, H.; Zhang, L. Microwave assisted synthesis of reduced graphene oxide incorporated MOF-derived ZnO composites for photocatalytic application. *Catal. Commun.* **2017**, 88, 5-8.
38. Umar, A.; Karunagaran, B.; Suh, E.K.; Hahn ,Y.B. Structural and optical properties of single-crystalline ZnO nanorods grown on silicon by thermal evaporation. *Nanotechnology* **2006**, 17, 4072-4077.
39. Dai, L.; Chen, X.L.; Wang, W.J.; Zhou, T.; Hu, B.Q. Growth and luminescence characterization of large-scale zinc oxide nanowires. *J. Phys.,Condens. Matter.* **2003**, 15, 2221-2226.
40. Yu, C.; Tong, Z.; Li, S.; Yin, Y. Enhancing the photocatalytic activity of ZnO by using tourmaline. *Mater. Lett.* **2019**, 240, 161-164.
41. Zhu, L.; Li, H.; Liu, Z.; Xia, P.; Xie, Y.; Xiong, D. Synthesis of the 0D/3D CuO/ZnO heterojunction with enhanced photocatalytic activity. *J. Phys. Chem. C* **2018**, 122, 9531-9539.
42. Zhao, Y.; Li, L.; Zuo, Y.; He, G.; Chen, Q.; Meng, Q.; Chen,H. Reduced graphene oxide supported ZnO/CdS heterojunction enhances photocatalytic removal efficiency of hexavalent chromium from aqueous solution. *Chemosphere* ***2022***, 286, 131738.
43. Shen, C.; Chen, Y.; Xu, X.; Li, X.; Wen, X.; Liu, Z.; Xing, R.; Guo, H.; Fei, Z. Efficient photocatalytic H_2 evolution and Cr (VI) reduction under visible light using a novel Z-scheme $SnIn_4S_8/CeO_2$ heterojunction photocatalysts. *J. Hazard. Mater.* **2021**, 416, 126217.
44. Zhang, J.; Zhang, R.; Cao, J.; Wang, Y.; Wang, F.; Wu, H. DFT-proved Z-type $ZnO/SnIn_4S_8$ heterojunction for detecting hexavalent chromium. *J. Alloy. Compd.* **2022**, 922, 166266.